

Field Panel Method

Documentation

Adrien Crovato

University of Liège - Department of Aerospace & Mechanical Engineering
Fluid-Structure Interactions & Experimental Aerodynamics
December 2017



Contents

I	Introduction	3
II	Theory	4
1	The Full Potential Equation	4
2	Panel Method	5
3	Field module	6
4	Influence coefficients	6
4.1	Surface AICs	6
4.2	Field AICs	8
III	Implementation	10
5	Organization of the code	10
6	Pre-processor and input files	12
6.1	Input files	12
6.2	Geometry handling	12
7	Solver	13
7.1	Subpaneling	13
7.2	AIC matrices assembly	14
7.3	Panel Method	14
7.4	Field variables computation	14
7.5	Minigrid	15
7.6	Supercritical flow handling	16
7.6.1	Derivative upwinding	16
7.6.2	Artificial density and artificial viscosity	16
7.7	Full solution procedure	17
8	Post-processor and output files	18
8.1	Output files	18
IV	Computational examples	18
9	Incompressible flow	19
10	Subcritical flow	19

11 Supercritical flow	20
12 Typical aircraft wing	20
13 Challenge and attempted solution	21
V Conclusion	22
References	23

Part I

Introduction

In the on-going effort to build more efficient aircraft, the minimization of the structural weight and the maximization of the aerodynamic efficiency usually lead to the design of very flexible and highly loaded composite wings. Aeroelasticity thus plays an increasingly important role in preliminary aircraft design. Current aeroelastic tailoring practice for early preliminary aircraft design relies on linear aerodynamic modeling, which is unable to predict shocks and boundary layers. One solution is to enhance the linear aerodynamic modeling methodology by supplementing the Panel Method with a field module. The resulting Field Panel Method is then able to predict transonic flowfields while having a low computational cost, thus allowing fast and reliable aerodynamic loads predictions for aeroelastic computations.

This document presents an implementation of the Field Panel Method developed at the University of Liège during the academic year 2016-2017. In the first part, the theory of the method is described. In the second part, the implementation of the method is detailed. Finally, some computational examples are given, illustrating the advantages of the method as well as its current limitations.

Part II

Theory

The first part of the present report describes the theory behind the Field Panel Method (FPM). The FPM can be considered as an extension of the Panel Method (PM) solving the Full (nonlinear) Potential Equation (FPE). First, the Panel Method will be described, then the way it is extended into the Field Panel Method will be explained.

1 The Full Potential Equation

The Full Potential Equation is obtained by assuming that the velocity, \mathbf{U} , derives from a scalar potential, ϕ . The continuity equation then reads,

$$\nabla \cdot (\rho \nabla \phi) = 0. \quad (1.1)$$

This form assumes that the flow is steady, inviscid and isentropic (hence irrotational). However, the nonlinearities are retained through the density,

$$\rho = \rho_\infty \left[1 + \frac{\gamma - 1}{2} M_\infty^2 (1 - (\nabla \phi)^2) \right]^{\frac{1}{\gamma - 1}}, \quad (1.2)$$

where M_∞ is the freestream Mach number.

The assumption of the flow being isentropic is fully valid outside of the boundary layer, which is very thin at high speed, and provided that the shockwaves present in the flow (if any) remain weak. Since the entropy production across a shockwave is proportional to $(1 - M_s)^3$, this approximation is usually considered to be valid if the maximum Mach number in front of the shockwave, M_s , is less than 1.3.

The FPE can be written in Poisson's form,

$$\begin{aligned} \nabla \cdot (\nabla \phi) &= \sigma, \\ \sigma &= \frac{\rho}{\rho_\infty} \nabla \rho \cdot \nabla \phi, \end{aligned} \quad (1.3)$$

and transformed through Green's third identity into,

$$\phi(x, y, z) = \phi_\infty - \underbrace{\frac{1}{4\pi} \int_{S_B} \left[\sigma \frac{1}{r} - \mu \mathbf{n} \cdot \nabla \left(\frac{1}{r} \right) \right] dS}_{\varphi_b} - \underbrace{\frac{1}{4\pi} \int_V \left[\sigma \frac{1}{r} \right] dV}_{\varphi_f}, \quad (1.4)$$

where r is the distance defined by $\sqrt{x^2 + y^2 + z^2}$ and \mathbf{n} is the unit normal vector to the surface of the geometry.

In Equation 1.4, the potential can be considered as the superimposition of a freestream potential ϕ_∞ , a surface induced potential φ_b , and a field induced potential φ_f . The freestream potential is given by an uniform, undisturbed flow at a given angle of attack. The surface induced potential is modeled by source singularities τ and doublet singularities μ . Their strength is computed by the

Panel Method. The field induced potential is modeled by field sources σ , which strength is given by the second Equation of 1.3.

In summary, the system of Equations 1.3 needs to be solved iteratively by a panel method and a field module.

2 Panel Method

The Panel Method solves the Linear Potential Equation (LPE),

$$\nabla\phi = 0. \quad (2.1)$$

Compared to the FPE, the LPE further assumes that the flow is incompressible and the continuity equation then becomes linear. Consequently, it can be solved by a Boundary Element Method (BEM) in which only the boundary of the geometry needs to be discretized. The theory concerning the PM described in the present document mainly comes from Katz & Plotkin^[1].

In the Panel Method, only the surface induced potential of Eq. 1.4 needs to be considered,

$$\phi(x, y, z) = \phi_\infty - \underbrace{\frac{1}{4\pi} \int_{S_B} \left[\tau \frac{1}{r} - \mu \mathbf{n} \cdot \nabla \left(\frac{1}{r} \right) \right] dS}_{\varphi_b}. \quad (2.2)$$

Since the perturbation potential rapidly decays when moving away from the body, the farfield boundary condition is automatically enforced by adding the freestream potential to the surface induced potential. On the other hand, since the flow is inviscid, the only remaining boundary condition is the impermeability of the surface of the geometry, that is (Neuman B.C.),

$$\nabla\phi_b \cdot \mathbf{n} = 0, \quad (2.3)$$

or (Dirichlet B.C.),

$$\phi_b = 0. \quad (2.4)$$

Following the Dirichlet boundary condition, the potential inside the geometry ϕ_i is also equal to zero. Moreover, the sources induce a discontinuity in the potential which is equal to $\frac{\partial(\phi - \phi_i)}{\partial n}$. Therefore, if source strengths are set to include the normal component of the freestream flow, the Dirichlet B.C. can be recast into,

$$\varphi_b = 0. \quad (2.5)$$

By discretizing the geometry into panels, onto which constant source and doublet singularities are placed, equations 2.2 and 2.5 can then be combined in discrete form, yielding,

$$\mathbf{A}\mu + \mathbf{B}\tau = 0, \quad (2.6)$$

where \mathbf{A} and \mathbf{B} are the influence coefficient matrices, depending solely on the geometry.

Finally, wake panels are added to impose the Kutta condition, required for the flow to smoothly leave the body and produce lift. These panels extend horizontally from the trailing edge to the farfield behind the wing. To accurately represent the physics, the wake panels should be shed and follow the

flow (thus representing a force-free wake) instead of being flat. However, flat wake and force-free wake produce very similar results for steady flows. Each wake panel contains a constant doublet singularity whose strength is equal to the difference of doublet strength of the trailing edge panels on the suction and the pressure side. These wake panels thus contain no additional unknowns and their influence coefficients can be included in the matrix \mathbf{A} .

3 Field module

The field module supplements the Panel Method and model the compressibility of the flow by taking into account the nonlinear terms in the right hand side of the Full Potential Equation written under Poisson's form (Eq. 1.3). The theory concerning the Field module of the FPM mainly comes from Gebhardt et al.^[2] and Chu et al.^[3].

The field module is used to compute the volume integral in Equation 1.4. To represent the sources σ , a rectangular parallelepipedic volume enclosing the nonlinearities in the flow around the geometry is defined. This volume is then divided into uniform cells to form a Cartesian, non body-conforming, grid. Each cell is treated as a field panel containing a constant source singularity distribution of strength σ . These singularities are iteratively computed according to the second equation in 1.3, in which the total potential in the field ϕ_f is computed by the discretized form of Equation 1.4,

$$\phi_f = \phi_\infty + \mathbf{A}_f \mu + \mathbf{B}_f \tau + \mathbf{C} \sigma, \quad (3.1)$$

where the surface singularities μ and τ are updated by the panel method. To close the iterative procedure and to respect the impermeability boundary condition, the surface source singularities must now include the normal component of the freestream velocity as well as the normal component of the velocity induced by the field sources. The new boundary condition reads,

$$\nabla \varphi_b \cdot \mathbf{n} = -\nabla(\phi_\infty + \varphi_f) \cdot \mathbf{n}. \quad (3.2)$$

4 Influence coefficients

This section gives the expression of the different Aerodynamic Influence Coefficients needed by the panel method.

4.1 Surface AICs

The influence coefficients for the velocity potential induced by surface panels were derived by Hess & Smith^[4].

Notations

The computations are carried in the (flat) panel reference frame shown in Figure 4.1, whose collocation point is noted (x_0, y_0) , corner points (numbered cyclically) are noted by (x_k, y_k) with $k = 1, 2, 3, 4$ and surface is noted S . The target point onto which the potential is sought is denoted by $P(x, y, z)$. In order to perform the change of frame of reference, the rotation matrix is used to pre-multiply the vector OP .

$$R = \begin{bmatrix} \mathbf{e}_x \cdot \mathbf{e}_X & \mathbf{e}_x \cdot \mathbf{e}_Y & \mathbf{e}_x \cdot \mathbf{e}_Z \\ \mathbf{e}_y \cdot \mathbf{e}_X & \mathbf{e}_y \cdot \mathbf{e}_Y & \mathbf{e}_y \cdot \mathbf{e}_Z \\ \mathbf{e}_z \cdot \mathbf{e}_X & \mathbf{e}_z \cdot \mathbf{e}_Y & \mathbf{e}_z \cdot \mathbf{e}_Z \end{bmatrix} \quad (4.1)$$

Where $\mathbf{e}_x, \mathbf{e}_y, \mathbf{e}_z$ is the reference frame attached to the panel and $\mathbf{e}_X, \mathbf{e}_Y, \mathbf{e}_Z$ is the inertial reference frame.

To simplify the expression of the influence coefficients, the following variables are defined,

$$d_{ij} = \sqrt{(x_j - x_i)^2 + (y_j - y_i)^2} \quad (4.2)$$

$$m_{ij} = \frac{y_j - y_i}{x_j - x_i} \quad (4.3)$$

$$r_k = \sqrt{(x - x_k)^2 + (y - y_k)^2 + z^2} \quad (4.4)$$

$$e_k = (x - x_k)^2 + z^2 \quad (4.5)$$

$$h_k = (x - x_k)(y - y_k). \quad (4.6)$$

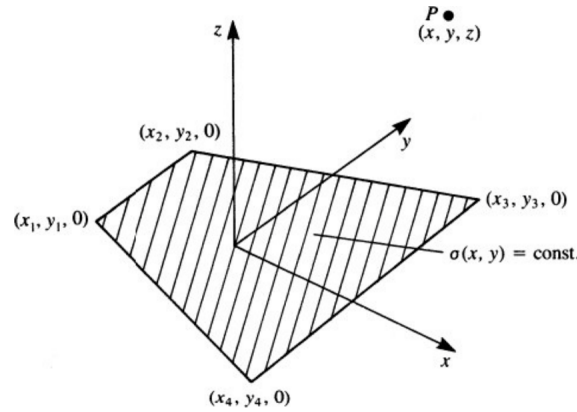


Figure 4.1: Panel and notations^[1].

Constant quadrilateral source

$$\begin{aligned}
\varphi_\tau = & \frac{-\tau}{4\pi} \left\{ \left[\frac{(x-x_1)(y_2-y_1) - (y-y_1)(x_2-x_1)}{d_{12}} \log \frac{r_1+r_2+d_{12}}{r_1+r_2-d_{12}} \right. \right. \\
& + \frac{(x-x_2)(y_3-y_2) - (y-y_2)(x_3-x_2)}{d_{23}} \log \frac{r_2+r_3+d_{23}}{r_2+r_3-d_{23}} \\
& + \frac{(x-x_3)(y_4-y_3) - (y-y_3)(x_4-x_3)}{d_{34}} \log \frac{r_3+r_4+d_{34}}{r_3+r_4-d_{34}} \\
& + \left. \frac{(x-x_4)(y_1-y_4) - (y-y_4)(x_1-x_4)}{d_{41}} \log \frac{r_4+r_1+d_{41}}{r_4+r_1-d_{41}} \right] \\
& - |z| \left[\arctan \left(\frac{m_{12}e_1 - h_1}{zr_1} \right) - \arctan \left(\frac{m_{12}e_2 - h_2}{zr_2} \right) \right. \\
& + \arctan \left(\frac{m_{23}e_2 - h_2}{zr_2} \right) - \arctan \left(\frac{m_{23}e_3 - h_3}{zr_3} \right) \\
& + \arctan \left(\frac{m_{34}e_3 - h_3}{zr_3} \right) - \arctan \left(\frac{m_{34}e_4 - h_4}{zr_4} \right) \\
& + \left. \left. \arctan \left(\frac{m_{41}e_4 - h_4}{zr_4} \right) - \arctan \left(\frac{m_{41}e_1 - h_1}{zr_1} \right) \right] \right\}. \tag{4.7}
\end{aligned}$$

Constant quadrilateral doublet

$$\begin{aligned}
\varphi_\mu = & \frac{\mu}{4\pi} \left[\arctan \left(\frac{m_{12}e_1 - h_1}{zr_1} \right) - \arctan \left(\frac{m_{12}e_2 - h_2}{zr_2} \right) \right. \\
& + \arctan \left(\frac{m_{23}e_2 - h_2}{zr_2} \right) - \arctan \left(\frac{m_{23}e_3 - h_3}{zr_3} \right) \\
& + \arctan \left(\frac{m_{34}e_3 - h_3}{zr_3} \right) - \arctan \left(\frac{m_{34}e_4 - h_4}{zr_4} \right) \\
& + \left. \arctan \left(\frac{m_{41}e_4 - h_4}{zr_4} \right) - \arctan \left(\frac{m_{41}e_1 - h_1}{zr_1} \right) \right]. \tag{4.8}
\end{aligned}$$

4.2 Field AICs

The influence coefficients for the potential and the velocity induced by field panels are taken respectively from Seidov & Skvirsky^[5] and Chu et al.^[3].

Notations

A rectangular parallelepipedic field cell is considered. The origin of the frame of reference is located at the cell center of gravity and the axes are aligned with respect to the cell edges. The field cell is bound by the planes $x = \xi_1$, $x = \xi_2$, $y = \eta_1$, $y = \eta_2$, $z = \zeta_1$ and $z = \zeta_2$. If the cell holds a constant source singularity of strength σ , the potential induced by this field cell at an arbitrary point $P(x, y, z)$ located inside or outside of the cell is given by,

$$\phi_\sigma(x, y, z) = \frac{-\sigma}{4\pi} \int_{\xi_1}^{\xi_2} \int_{\eta_1}^{\eta_2} \int_{\zeta_1}^{\zeta_2} \frac{1}{\sqrt{(x-\xi)^2 + (y-\eta)^2 + (z-\zeta)^2}} d\zeta d\eta d\xi. \tag{4.9}$$

To simplify the result of this integral, the following variables are defined,

$$A = x - \xi_i \quad (4.10)$$

$$B = y - \eta_j \quad (4.11)$$

$$C = z - \zeta_k \quad (4.12)$$

$$R = \sqrt{A^2 + B^2 + C^2}. \quad (4.13)$$

Potential

$$\begin{aligned} \varphi_\sigma = \frac{-\sigma}{4\pi} \sum_{i,j,k=1}^2 (-1)^{i+j+k} & \left[BC \log(A+R) - \frac{A^2}{2} \arctan \frac{BC}{AR} \right. \\ & + CA \log(B+R) - \frac{B^2}{2} \arctan \frac{CA}{BR} \\ & \left. + AB \log(C+R) - \frac{C^2}{2} \arctan \frac{AB}{CR} \right] \end{aligned} \quad (4.14)$$

Velocities

$$u_{x,\sigma} = \frac{\partial \phi_\sigma}{\partial x} = \frac{\sigma}{4\pi} \sum_{i,j,k=1}^2 (-1)^{i+j+k} \left[\frac{B}{2} \log \frac{(R+C)}{R-C} + \frac{C}{2} \log \frac{(R+B)}{R-B} - A \arctan \frac{BC}{AR} \right] \quad (4.15)$$

$$u_{y,\sigma} = \frac{\partial \phi_\sigma}{\partial y} = \frac{\sigma}{4\pi} \sum_{i,j,k=1}^2 (-1)^{i+j+k} \left[\frac{C}{2} \log \frac{(R+A)}{R-A} + \frac{A}{2} \log \frac{(R+C)}{R-C} - B \arctan \frac{CA}{BR} \right] \quad (4.16)$$

$$u_{z,\sigma} = \frac{\partial \phi_\sigma}{\partial z} = \frac{\sigma}{4\pi} \sum_{i,j,k=1}^2 (-1)^{i+j+k} \left[\frac{A}{2} \log \frac{(R+B)}{R-B} + \frac{B}{2} \log \frac{(R+A)}{R-A} - C \arctan \frac{AB}{CR} \right] \quad (4.17)$$

Part III

Implementation

In this part of the document, the general organization of the implementation of the Field Panel Method is first described. Then, the main features of the implementation are given.

5 Organization of the code

The code has been written in the high-level, scientific and efficient C++ language. Extensive usage of structures has been made to keep the code organized and simple to use. The matrices are handled by the user-friendly Eigen library^[6]. Globally, the code is fairly modular and can be modified quite easily if further development is needed.

The code is split into 3 main blocks: a pre-processor, a solver and a post-processor. The pre-processor reads the user provided data, such as the grid points and the flow conditions, and creates the matrices required by the solver. The solver first assembles the AIC matrices and iteratively calls the panel method and the field module to solve the flow. The post-processor outputs the computed flow variables into readable ASCII files.

Figure 5.1 illustrates the main blocks of the code as well as the different functions. They will be further described in the next sections.

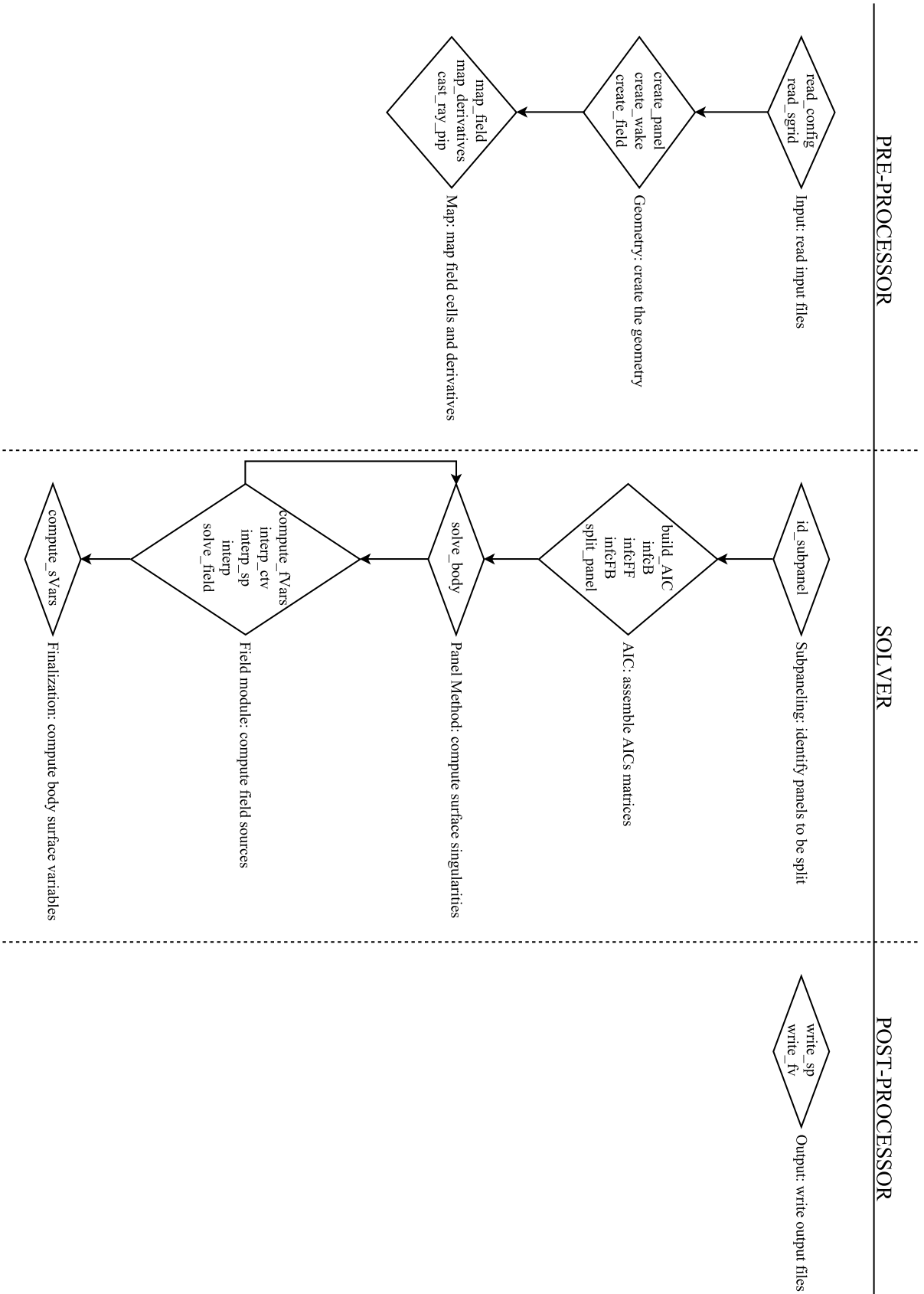


Figure 5.1: Code flowchart.

6 Pre-processor and input files

6.1 Input files

The code relies on two ASCII input files. The first is a `.cfg` file containing the freestream flow quantities (Mach number and angle of attack) as well as the domain and the Cartesian grid definition parameters. The second file (`.pts`) contains the points defining the geometry to be analyzed. These points need to be provided in a structured way. The geometry is divided into (spanwise) stations. Then, the points defining these stations are written in counter-clockwise order, starting from the trailing edge. The first 2 numbers written at the beginning of the file (before the list of points) give the number of points in a station and the number of stations.

6.2 Geometry handling

The main operation performed in the pre-processor is the creation of the surface and field panels and their storage into matrices. The surface panels are flat quadrilateral surfaces defined by their 4 corner points, their center of gravity, and 3 unit orthogonal vectors (longitudinal, transverse and normal). Each of these quantities are stored into matrices. For example, the unit normal vectors are stored into a $p \times 3$ matrix, where p is the total number of panel and the x , y and z components are stored in the different columns. The field panels are defined by their center of gravity and the cell size in the x , y and z directions. Note that the mesh is uniform, *i.e.* the field panels all have the same size. The surface and the field matrices are regrouped into 2 structures (`BODY` and `FIELD`). If the code needs to be extended to handle several networks of surface (or field) panels, these structures can be easily vectorized.

The second operation performed by the pre-processor is the mapping of the field. Since the volume grid is Cartesian and does not conform to the body, cells lying inside the body (*i.e.* internal cells) must be distinguished from cells outside the body (*i.e.* external cells). Moreover, two adjacent (external) cells may be separated by a wake surface or several body surfaces. This will be problematic when using finite differences to compute the derivatives of the potential in the field and obtain the source term, since the potential is discontinuous across these surfaces. In order to deal with this problem while allowing complex geometries to be handled, several techniques can be used, such as: jump relations, minigrid and cell sorting algorithm. The first technique consists in identifying cells adjacent to any surface and implementing jump relations inside the finite differences. In this way, the discontinuity in the potential is taken into account. The second technique will be described in one of the following paragraphs. Finally, the third technique, which has been used in the present code, consists in identifying the problematic cells and preventing the derivative in the given direction. In order to identify the situation of a cell, a 3D adaptation of the Point In Polygon (PIP) algorithm is used.

To check if the cell is inside or outside the body, the following algorithm is used:

- Cast a ray from the center of the cell in the x -direction (to infinity)
- Count the number of panels the ray pierces
 - Check if the ray is not parallel to the plane containing the panel
 - Check if the ray intersects this plane and compute the intersection

- Check that this intersection is included in the panel
- If the number of valid intersections is even, the point lies outside the body

To check if the derivative can be computed in a given direction for any external cell, The above algorithm is also used, except that the ray is cast from the center of the cell to the center of adjacent cells. If one valid intersection is detected, the derivative in the given direction is immediately prevented.

7 Solver

The solver mainly consists of an iterative loop including the Panel Method and the field module. Before entering in the loop, the AICs matrices are assembled and the different variables are initialized.

7.1 Subpaneling

Figure 7.1 illustrates the effect of the subpaneling technique by showing the x-component of the velocity at cells center located just above a NACA0012 wing. For large cell sizes, the solution is not converged and the mesh must be refined. However, when the cell size is too small, oscillations caused by the discontinuity in the surface singularities across body panels start to appear. Since the velocity is used to compute the source term, which will in turn correct the panel method and drive the solution process, these oscillations can lead to the divergence of the algorithm. These oscillations can be effectively removed by the subpaneling technique, which is an adaptation of the subvortex technique proposed by Maskew in 1977^[7]. It consists in using a local, linear singularity strength distribution instead of constant singularity values on each panel.

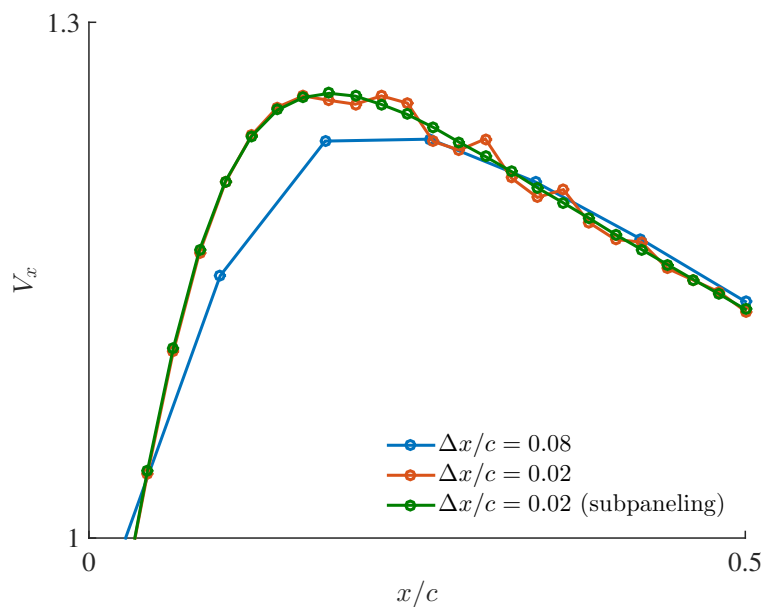


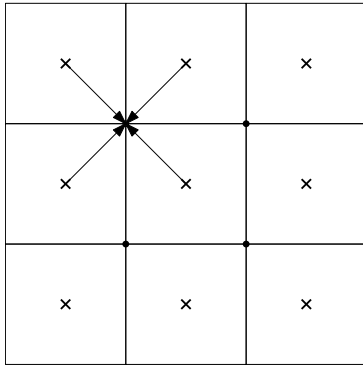
Figure 7.1: Grid size and subpaneling effect on velocity for near-field cells.

In practice, the subpaneling is performed in 2 steps. First, if a field cell center is located too close to the surface of the body, the panel is split into a user defined number of subpanels (with constant singularity strength). Then, at each iteration, when the singularity strength is known on each panel,

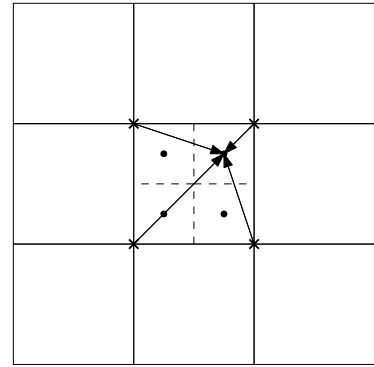
the singularity is interpolated linearly on the subpanels. The bilinear interpolation, also performed in 2 steps, is illustrated on Figure 7.2. The contribution to the potential in the field at cell i by the panel j (split in n_s subpanels) can then be computed as,

$$\varphi_f|i, j = \sum_k^{n_s} A_{f,k} \mu_k + B_{f,k} \tau_k, \quad (7.1)$$

where k is the subpanel index.



(a) Panel centers to panel vertices.



(b) Panel vertices to subpanel centers.

Figure 7.2: Singularity bilinear interpolation on subpanels.

7.2 AIC matrices assembly

An important step in the (Field) Panel Method is the assembly of the Aerodynamic Influence Coefficients matrices. This is performed once before the iteration loop and these coefficients can be reused later for other purposes, such as optimization. The FPM needs 4 groups of matrices, each stored into different structures: body-to-body, body-to-field, field-to-field and field-to-body AICs. Each element of these matrices represents the influence of a panel onto another and depends solely on geometric parameters. Note that the size of the matrices grows as N^2 , where N is the number of panels. The number of panels should therefore be kept to a minimum.

When a body-to-field AIC of a panel that will be split needs to be computed, this AIC is set to 0 instead and the AICs of the corresponding subpanels are stored into another matrix. The AIC matrices related to the subpanels are regrouped into a fifth structure.

7.3 Panel Method

The panel method is part of the iterative loop. At each iteration, the surface source singularities are set to fulfill the modified impermeability condition on the body surface (Eq. 3.2). With the sources and the AICs being known, the linear system (Eq. 2.6) can be solved to obtain the surface doublets.

7.4 Field variables computation

The field module is also part of the iterative loop. In the present implementation, it has been split into 2 parts. The first part is responsible for the computation of the velocity and its related variables (density and Mach number) in the field. The role of the second part is to compute the derivative of the density to obtain the field sources.

Several options exist to compute the velocity in the field. Either, the potential can be computed first

with Aerodynamic Influence Coefficients, then differentiated with finite differences on the Cartesian grid,. Or the velocity can be computed directly with the AICs (these AICs are established analytically). Both approaches have been implemented and tested in the present work.

The second approach is more accurate, but it involves the computation of three AIC matrices instead of one (three components of the velocity instead of a scalar potential). Moreover, near the body surface, the discontinuity between the singularity values on each panel induces oscillations in the velocity distribution in the field, despite the subpaneling technique. On the other hand, if a sufficiently fine grid is used, the finite differences of the potential give a very good approximation of the velocity computed directly with the AICs. For all of these reasons, the potential formulation (potential computed with the AICs and differentiated with finite differences) has been retained in the present work.

The computation of the potential on the field is quite straightforward. However, the Equation 3.1 must be slightly modified to include the subpanels contribution. With the potential being known on the field panels, the velocity can be derived by using finite differences. The density and the Mach number can then be computed thanks to the isentropic formula. When the density is known, it can be derived with finite differences to compute the field sources strength. The very last step is to compute the field sources induced velocity on the surface of the geometry with appropriate AICs.

7.5 Minigrid

In order to compute the derivatives in the field, the simplest approach it to use finite differences on the Cartesian grid. However, to increase the accuracy and to prevent the derivatives from passing through the surface of the body or the wake, a minigrid technique, proposed by Gebhardt et al. [2], can be used.

The minigrid technique consists in calculating the potential at several points inside a cell and computing the derivatives from these points. In practice, the size of the minigrid is small compared to the cell ($\Delta x_{MG} = 0.001 \times \Delta x$) so that the derivatives do not intersect the body or wake surfaces. Using a minigrid with such as small size is equivalent to computing the velocity directly the AICs rather than using finite differences. On a minigrid, a typical derivative is computed as (see Fig. 7.3b),

$$\frac{\partial \varphi_f}{\partial x} \Big|_{i,j} \simeq \frac{\varphi_f \Big|_{i+\Delta x_{MG},j} - \varphi_f \Big|_{i-\Delta x_{MG},j}}{2\Delta x_{MG}}, \quad (7.2)$$

Instead of (see Fig. 7.3a),

$$\frac{\partial \varphi_f}{\partial x} \Big|_{i,j} \simeq \frac{\varphi_f \Big|_{i+1,j} - \varphi_f \Big|_{i-1,j}}{2\Delta x}. \quad (7.3)$$



Figure 7.3: Grid types to compute derivatives.

Despite its advantages, the minigrid has two major drawbacks. The first is that the potential has to be computed in several points inside the cell, hence requiring more than one AIC per cell (7 AICs are required in 3D instead of 1 for a regular grid). The second drawback is that the oscillations in the velocity close to the body caused by the discontinuity between the surface singularities are amplified by the minigrid. Compared to the minigrid, the regular grid is coarser, it thus tends to smooth the derivatives. Moreover, the accuracy of the results obtained on a coarse minigrid and on a relatively fine regular grid (both grids were chosen to have the same computational cost) is almost the same. To avoid the oscillations in the solution and to simplify the implementation, the regular grid approach has been retained in the present work.

7.6 Supercritical flow handling

When the flow is supersonic, the information, traveling at the speed of sound in the fluid, cannot propagate upstream. Consequently, the equation, elliptic in a subsonic flow, becomes hyperbolic in a supersonic flow. In the finite difference/element/volume methods, this change of physics should be reflected by a change in the derivative discretization scheme. In the present work, three techniques have been tested: derivative upwinding, artificial density and artificial viscosity.

7.6.1 Derivative upwinding

The simplest way to reflect the hyperbolic character of the equation is to use central differences in subsonic regions and backward (upwind) differences in the supersonic region. The method converges but the accuracy can be improved. Actually, in order to properly upwind the derivatives, backward derivatives should be used in the local (streamline) direction of the flow. This condition gave rise to the rotated difference scheme implemented by Jameson^[8].

7.6.2 Artificial density and artificial viscosity

Under the rotated difference scheme, an artificial density or viscosity is effectively introduced in the solution. The artificial density is computed as,

$$\tilde{\rho} = \rho - \mu \frac{\partial \rho}{\partial s} \Delta s, \quad (7.4)$$

where $\mu = \max\left(0, 1 - \frac{1}{M^2}\right)$ (M is the local Mach number) and s is the local (streamline) direction of the flow.

The derivative of ρ is usually approximated by,

$$\frac{\partial \rho}{\partial s} \Delta s = \frac{1}{\sqrt{u^2 + v^2 + w^2}} \left(u \frac{\partial \rho}{\partial x} \Delta x + v \frac{\partial \rho}{\partial y} \Delta y + w \frac{\partial \rho}{\partial z} \Delta z \right), \quad (7.5)$$

where u , v and w are the x , y and z components of the velocity and Δx , Δy and Δz are the local cell sizes in the x , y and z directions.

To be consistent with the hyperbolic physics, the derivatives of the density should be upwinded. Further details can be found in Hafez et. al.^[9].

In a very similar way, an artificial viscosity can be directly added to the field source term (as shown by Rottegermann and Wagner^[10]),

$$\tilde{\sigma} = \sigma + \mu \frac{\partial \sigma}{\partial s} \Delta s. \quad (7.6)$$

In the present work, both approaches have been tested and yielded similar results. The artificial viscosity approach has been retained since it is more practical to implement.

7.7 Full solution procedure

This section describes the solution procedure currently implemented. Note that the field variables are computed by setting that magnitude of the freestream velocity to $V_\infty = 1$.

Initialization

After the geometry preprocessing, the matrices containing the influence coefficients are computed: body to body (\mathbf{A} and \mathbf{B}), field to field (\mathbf{C}), body to field (\mathbf{A}_f and \mathbf{B}_f) and field to body ($\mathbf{C}_{x,b}$, $\mathbf{C}_{y,b}$, $\mathbf{C}_{z,b}$). All the relevant variables (like $\tilde{\sigma}$ and $u_{n,\sigma}$) are also initialized to zero.

Step 1 - Surface sources

The first step of the iterative process consists in setting the surface source singularities τ to $-(\mathbf{V}_\infty \cdot \mathbf{n} + u_{n,\sigma})$ so that they include the non-lifting normal velocity component, according to Eq. 3.2.

Step 2 - Surface doublets

The next step consists in solving the linear system of equations $\mathbf{A}\mu + \mathbf{B}\tau = 0$ to obtain the surface doublet singularities, μ .

Step 3 - Field variables

The next step consists in computing the different field variables. The total potential in the field is computed from $\phi_f = \phi_\infty + \mathbf{A}_f\mu + \mathbf{B}_f\tau + \mathbf{C}\tilde{\sigma}$, and differentiated to obtain the velocity in the field $\mathbf{V}_f = [u_{x,f}, u_{y,f}, u_{z,f}]$. The speed of sound a , the Mach number M and the density ratio $\frac{\rho}{\rho_\infty}$ are then computed thanks to the following (isentropic) relations:

$$\begin{aligned} a^2 &= a_\infty^2 + \frac{\gamma - 1}{2} - \frac{\gamma - 1}{2} \mathbf{V}_f^2 \\ M &= \frac{V_f}{a} \\ \frac{\rho}{\rho_\infty} &= \left[1 + \frac{\gamma - 1}{2} M_\infty^2 (1 - \mathbf{V}_f^2) \right]^{\frac{1}{\gamma - 1}}. \end{aligned} \quad (7.7)$$

Step 4 - Field sources

The next step consists in updating the field source singularities according to $\sigma = \nabla \left(\frac{\rho}{\rho_\infty} \right) \cdot \mathbf{V}_f$. The artificial viscosity is then added using Eq. 7.6.

Step 5 - Boundary condition update

The normal component of the field source induced velocity can now be recomputed as $u_{n,\sigma} = [C_{x,b}\tilde{\sigma}, C_{y,b}\tilde{\sigma}, C_{z,b}\tilde{\sigma}] \cdot \mathbf{n}$

Step 6 - Stopping criterion

Steps 1 to 5 are repeated until convergence. The stopping criterion is defined as $\max |\tilde{\sigma}^n - \tilde{\sigma}^{n-1}| < \epsilon$, where n is the iteration counter and ϵ is a user-defined tolerance.

Finalization

The last step is to compute the surface velocity and the pressure coefficient. The surface velocity is the sum of the freestream velocity \mathbf{V}_∞ , the surface perturbation velocity \mathbf{u}_b and the field perturbation velocity \mathbf{u}_f . The latter has already been calculated to update the boundary condition. The surface perturbation velocity can be computed by differentiating the potential on the surface. If l , m and n are the axes of the frame attached to a panel, then

$$\begin{aligned} u_{l,b} &= -\frac{\partial \mu}{\partial l} \\ u_{m,b} &= -\frac{\partial \mu}{\partial m} \\ u_{n,b} &= \tilde{\sigma}. \end{aligned} \tag{7.8}$$

The obtained velocity vector is then rotated to the global axis and used to compute the total surface velocity,

$$\mathbf{V}_b = \mathbf{V}_\infty + \mathbf{u}_b + \mathbf{u}_f. \tag{7.9}$$

The pressure coefficient can subsequently be computed as,

$$C_p = \frac{2}{\gamma M_\infty^2} \left\{ \left[1 + \frac{\gamma-1}{2} M_\infty^2 (1 - V_b^2) \right]^{\frac{\gamma}{\gamma-1}} - 1 \right\}. \tag{7.10}$$

8 Post-processor and output files

8.1 Output files

The results produced by the FPM are written in 2 ASCII formatted .DAT files. One file contains the coordinates of the center of all body panels as well as the corresponding pressure coefficient. The other file contains the coordinates of the center of all field cells as well as the corresponding field variables. Additionally, the code generates 2 ASCII .POS files, containing the Mach number in the field and the pressure coefficient on the wing surface. They can be viewed using gmsh, a free open-source cross-platform software.

Part IV

Computational examples

In this part, the implemented FPM is illustrated on several computational examples to demonstrate its accuracy and its range of validity.

9 Incompressible flow

Figure 9.1 shows the pressure distribution at the mean aerodynamic chord of the NACA0012 and the Onera M6 wings at incompressible airspeed (Mach 0). The results for lifting and nonlifting flows perfectly match those obtained with `Panair`, hence demonstrating the validity of the implemented Panel Method.

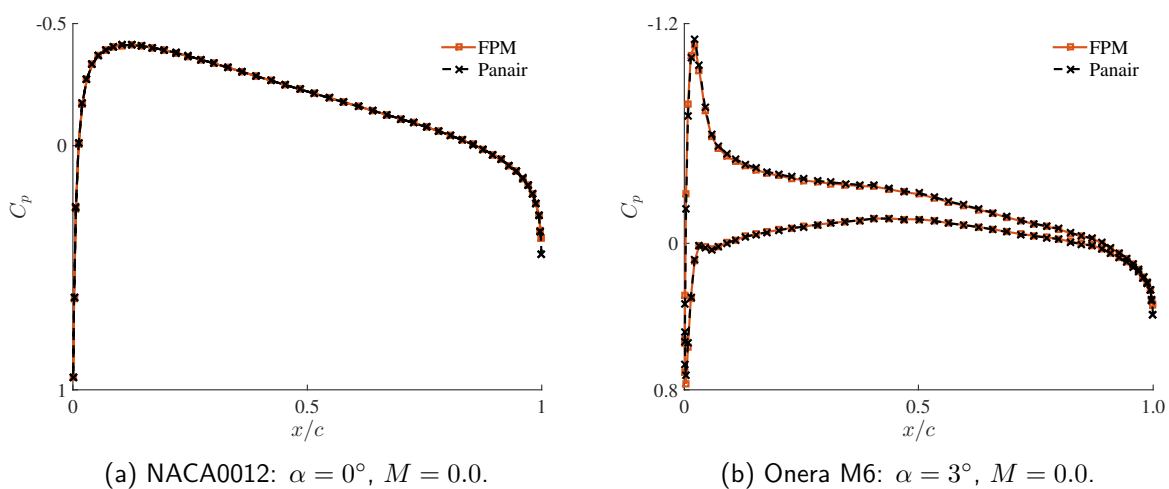


Figure 9.1: Pressure distribution around NACA0012 and Onera M6 at incompressible speed.

10 Subcritical flow

Figure 10.1 shows the pressure distribution around the NACA0012 and the Onera M6 submersed in a compressible flow. The angle of attack of the NACA0012 is set to 0° to obtain a nonlifting flow while the angle of attack of the M6 is set to 2° . The Mach number is chosen so that the flow remains subcritical for both wings.

Globally, the FPM shows excellent agreement with `Tranair` except near the suction peak, which is underestimated. The solution is also improved compared to `Panair`.

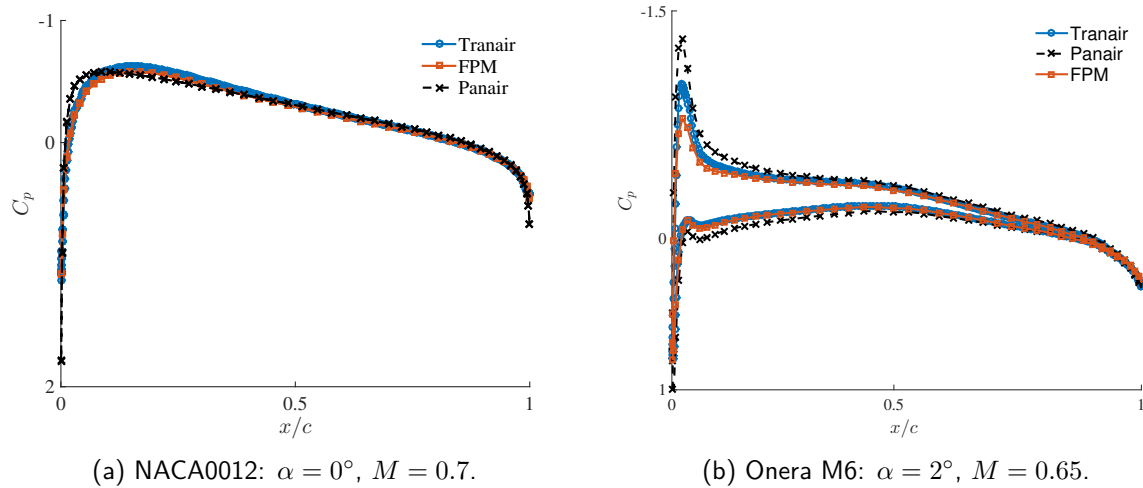


Figure 10.1: Pressure distribution around NACA0012 and Onera M6 at subcritical speed.

11 Supercritical flow

Figure 11.1 shows the pressure distribution around the NACA0012 and the Onera M6 submersed in a compressible flow. The angle of attack of the NACA0012 is set to 0° to obtain a nonlifting flow while the angle of attack of the M6 is set to 3° . The Mach number is chosen so that the flow becomes supercritical for both wings.

When the flow exhibits a shock, the accuracy of the method is degraded. Figs. 11.1a and 11.1b both show that the FPM tend to predict a smeared shock displaced upstream compared to Tranair's full potential solution. Fig. 11.1a also shows that the present solution follows the same trend than the solution obtained by Gebhardt et al.^[2] (the last known people to have worked on a Field Panel implementation). Even if the FPM solution shows significant improvement over the linear potential solution predicted by Panair, this is at the cost of the computational time and memory required to compute and store the AICs. A Fast Multipole Method could be implemented to reduce the computational requirements for transonic flows.

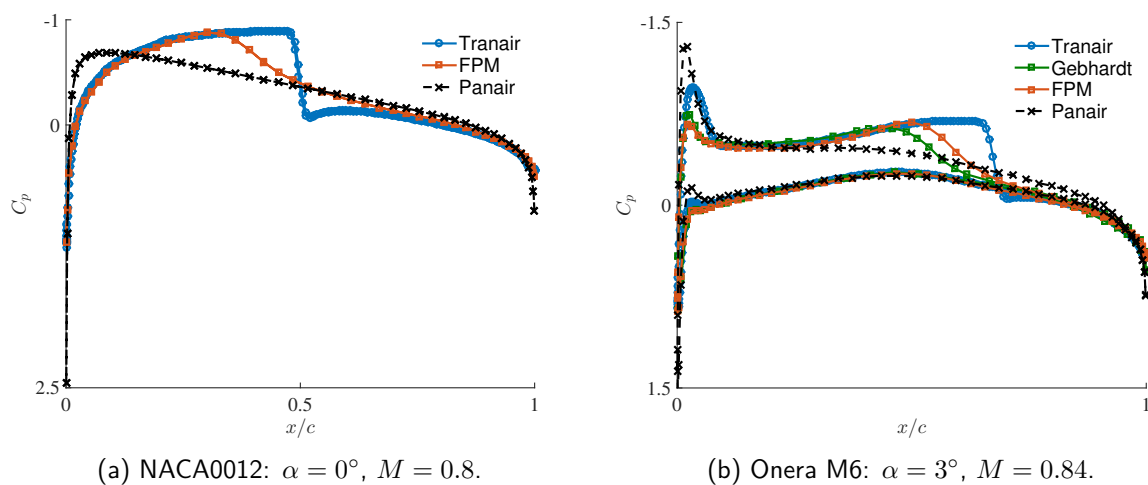


Figure 11.1: Pressure distribution around NACA0012 and Onera M6 at supercritical speed.

12 Typical aircraft wing

The last computational example to be studied in the present work is a typical business aircraft wing. The wing features a NASA SC(2)-0712 supercritical airfoil, a taper ratio of 0.4, a leading edge sweep angle of 25° and a dihedral angle of 5° . The tip airfoil is also twisted of -2° to create a washout. The span of the wing is 8m.

Figure 12.1 shows the pressure distributions around the wing computed by Tranair, the FPM and Panair at a Mach number of 0.79. The angles of attack used in the different models have been set to produce a lift coefficient of 0.4. They are respectively -1.3° , -1° , and -1.7° . At this Mach number, the flow is supercritical, but the shocks are still weak (the maximum Mach number in front of the shock is around 1.2). The FPM solution is rather close to Tranair solution despite the smearing of the shock. It is also improved compared to the linear potential Panair solution.

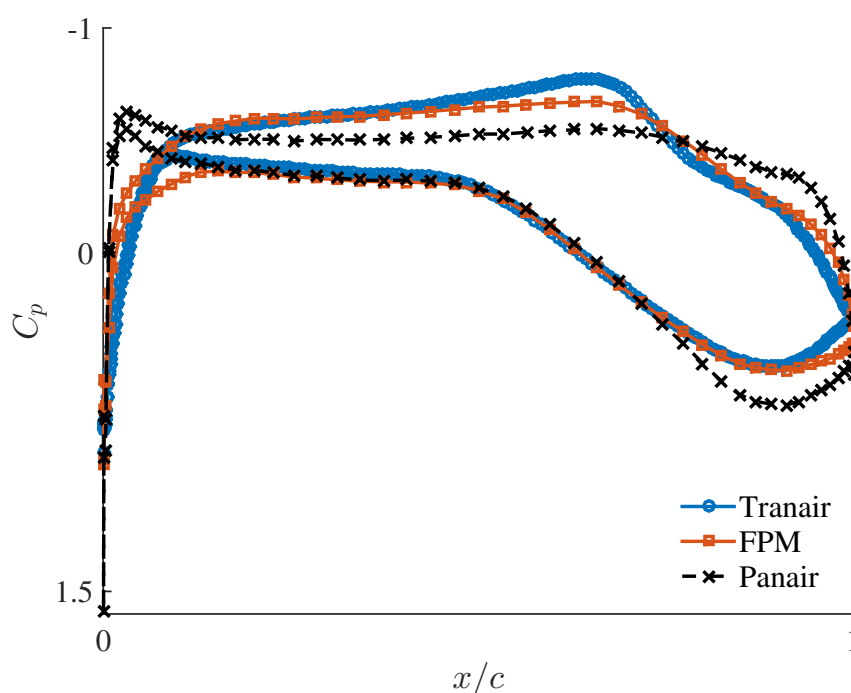


Figure 12.1: Pressure distribution around the NASA SC(2)-0712 wing at supercritical speed.

13 Challenge and attempted solution

As shown in Figure 11.1, the current implementation tends to smear the pressure peak at the leading edge and to displace and smear the shock.

The smearing of the pressure peak only happens on certain geometries (*e.g.* it is clearly visible on the Onera M6, but nearly absent on a NACA0012 wing) and, hence, could be due to an insufficient local grid refinement. Moreover, the pressure peak is still captured and its smearing does not influence too much the pressure distribution.

The impossibility to capture the shock properly poses a serious problem though. Several solutions have been attempted among which, an adaptation of the artificial viscosity, and an adaptation of the AIC matrices. The adaptation of the artificial viscosity consisted in scaling the μ factor in Eq. 7.6

by the magnitude of the gradient of the density. The adaptation of the AIC matrices consisted in removing the coefficients of influencing panels or cells located upstream of the target cell. However, both solutions failed.

Part V

Conclusion

The goal of the Field Panel Method implementation presented in this document is to solve compressible aeronautical flows quickly.

In the first part of the report, the theory and the formulation of the Field Panel Method were presented. The FPM has been chosen to solve the Full Potential Equation because it only needs to rely on a (non conforming) Cartesian grid to predict transonic aeronautical flows with weak shocks. Moreover, the computed Aerodynamic Influence Coefficients can be reused later for optimization.

In the second part, the implementation of the method was described. The main choices and features of the code, such as the potential formulation, the subpaneling technique and the artificial viscosity were also detailed.

Finally, in the last part, computational examples were given. The FPM was first compared to Panair's linear potential and Tranair's full potential solutions on the NACA0012 and the Onera M6 in incompressible, subcritical and supercritical conditions. The comparison in an incompressible flow allowed to validate the implementation of the Panel Method. For a subcritical flow, the agreement between the different solutions is excellent, except near the pressure peak, which tend to be underestimated by the Field Panel Method. This could be due to an insufficient local grid refinement. When the flow is supersonic, the solution is improved compared to the linear potential prediction but the captured shock tends to be displaced upstream and smeared. In order to reduce the computational requirements for transonic flows, a Fast Multipole Method could be implemented. This would enable the FPM to remain competitive with the Panel Method and allow it to be used in aeroelastic tailoring for preliminary aircraft design.

References

- [1] J. Katz and A. Plotkin. *Low-Speed Aerodynamics*. Cambridge Aerospace Series. Cambridge University Press, 2001.
- [2] Lutz Gebhardt, Dmitri Fokin, Thorsten Lutz, and Siegfried Wagner. An implicit-explicit dirichlet-based field panel method for transonic aircraft design. *AIAA Journal*, (June):1–13, 2002.
- [3] Li-chuan Chu, E Yates, and O Kandil. Integral equation solution of the full potential equation for transonic flows. In *27th Aerospace Sciences Meeting*, 1989.
- [4] J.L. Hess and A.M.O. Smith. Calculation of potential flow about arbitrary bodies. *Progress in Aerospace Sciences*, 8:1 – 138, 1967.
- [5] Z.F. Seidov and P.I. Skvirsky. Gravitational potential and energy of homogeneous rectangular parallelepiped. February 2000.
- [6] Gaël Guennebaud, Benoît Jacob, et al. Eigen v3. <http://eigen.tuxfamily.org>, 2010.
- [7] Maskew Brian. Subvortex technique for the close approach to a discretized vortex sheet. *Journal of Aircraft*, 4(2), February 1977.
- [8] Jameson Antony. Transonic potential flow calculations using conservation form. *Courant Institute of Mathematical Science*.
- [9] M Hafez, E Murman, and J South. Artificial compressibility methods for numerical solutions of transonic full potential equation. *11th Fluid and PlasmaDynamics Conference*, 17(8):838–844, 1978.
- [10] A Rottegermann and Siegfried Wagner. Cost Efficient Calculation of Compressible Potential Flow Around a Helicopter Rotor Including Free Vortex Sheet. (October):1–10, 1994.